

PAPER

## Energy-efficient miniature-scale heat pumping based on shape memory alloys

To cite this article: Hinnerk Ossmer *et al* 2016 *Smart Mater. Struct.* **25** 085037

View the [article online](#) for updates and enhancements.

### You may also like

- [Elastocaloric effects of carbon fabric-reinforced shape memory polymer composites](#)  
Seok Bin Hong, Yongsan An and Woong-Ryeol Yu
- [Elastocaloric effect of shape memory polymers in elastic response regime](#)  
Takamasa Hirai, Koichiro Uto, Mitsuhiro Ebara *et al.*
- [A single long NiTi tube compressive elastocaloric regenerator: experimental results](#)  
Siyuan Cheng



**UNITED THROUGH SCIENCE & TECHNOLOGY**

 **The Electrochemical Society**  
Advancing solid state & electrochemical science & technology

**248th  
ECS Meeting**  
Chicago, IL  
October 12-16, 2025  
*Hilton Chicago*

**Science +  
Technology +  
YOU!**

**SUBMIT  
ABSTRACTS by  
March 28, 2025**

**SUBMIT NOW**

# Energy-efficient miniature-scale heat pumping based on shape memory alloys

Hinnerk Ossmer<sup>1</sup>, Frank Wendler<sup>1</sup>, Marcel Gueltig<sup>1</sup>, Franziska Lambrecht<sup>1</sup>,  
Shuichi Miyazaki<sup>2</sup> and Manfred Kohl<sup>1</sup>

<sup>1</sup>Institute of Microstructure Technology, Karlsruhe Institute of Technology, PO Box 3640, D-76021 Karlsruhe, Germany

<sup>2</sup>Division of Materials Science, University of Tsukuba, Tsukuba, Ibaraki 305-8573, Japan

E-mail: [hinnerk.ossmer@kit.edu](mailto:hinnerk.ossmer@kit.edu)

Received 5 February 2016, revised 10 May 2016

Accepted for publication 11 May 2016

Published 19 July 2016



## Abstract

Cooling and thermal management comprise a major part of global energy consumption. The by far most widespread cooling technology today is vapor compression, reaching rather high efficiencies, but promoting global warming due to the use of environmentally harmful refrigerants. For widespread emerging applications using microelectronics and micro-electro-mechanical systems, thermoelectrics is the most advanced technology, which however hardly reaches coefficients of performance (COP) above 2.0. Here, we introduce a new approach for energy-efficient heat pumping using the elastocaloric effect in shape memory alloys. This development is mainly targeted at applications on miniature scales, while larger scales are envisioned by massive parallelization. Base materials are cold-rolled textured  $\text{Ti}_{49.1}\text{Ni}_{50.5}\text{Fe}_{0.4}$  foils of 30  $\mu\text{m}$  thickness showing an adiabatic temperature change of  $+20/-16$  K upon superelastic loading/unloading. Different demonstrator layouts consisting of mechanically coupled bridge structures with large surface-to-volume ratios are developed allowing for control by a single actuator as well as work recovery. Heat transfer times are in the order of 1 s, being orders of magnitude faster than for bulk geometries. Thus, first demonstrators achieve values of specific heating and cooling power of 4.5 and 2.9  $\text{W g}^{-1}$ , respectively. A maximum temperature difference of 9.4 K between heat source and sink is reached within 2 min. Corresponding COP on the device level are 4.9 (heating) and 3.1 (cooling).

Keywords: elastocaloric effect, heat pumping, solid state cooling, shape memory alloy, superelasticity

(Some figures may appear in colour only in the online journal)

## 1. Introduction

A considerable share of global energy consumption is associated with heating, ventilation, air conditioning and refrigeration (HVAC). As an example, in 2013 HVAC accounted for about 38% of the primary energy consumption in buildings of the United States [1]. The most common cooling and heat pumping technology today is vapor compression, reaching efficiencies of about 60% of the maximum possible Carnot efficiency [2]. However, commonly used working fluids are environmentally harmful as they contribute to greenhouse gas emission.

Another global trend affecting global energy consumption is the ongoing miniaturization of electronic components and the unprecedented increase of functionality on small scales, which allows for the development and widespread use of smart consumer devices and systems. Microtechnology and corresponding micro-electro-mechanical systems (MEMS) have become mature enabling various new applications such as novel sensor devices, autonomous sensor networks, medical devices and lab-on-a-chip systems [3, 4]. One problem in these systems is the local generation of enormous heat that needs to be dissipated. This requires efficient thermal management on a local scale, like cooling of hot spots on

microelectronic chips or temperature control of chip-scale analysis systems [5, 6]. In this realm, compressor technology is not useful due to limited miniaturization capability. Thermoelectrics is currently the most advanced technology that shows good miniaturization potential as no fluids or moving parts are required [7, 8]. Though, despite almost two decades of intensive research, device coefficients of performance (COP) are still low and hardly exceed a value of 2 [2, 9, 10].

For these reasons, research on alternative technologies is becoming increasingly important. In recent years, solid-state heat pumping using ferroic materials has been recognized to be a promising alternative due to its environmental compatibility and its potential to save energy [11–16]. A report commissioned by the US Department of Energy recently rated elastocaloric (or thermoelastic) cooling as most promising non-vapor-compression HVAC approach [1]. Elastocaloric shape memory alloy (SMA) foils and novel SMA films have been developed and investigated showing similar adiabatic temperature change compared to their bulk counterparts [17–21]. TiNiFe foils with rolling-induced texture have been shown to reach an adiabatic temperature change of 16 K and material COP of 10.5 [22]. First macroscale demonstrator developments show the potential as well as the critical issues of the elastocaloric cooling approach [14, 23–28]. Owing to the dimensions of the active material involved, however, large actuation forces are required for elastocaloric cycling. This drawback loses significance upon miniaturization. One important issue is reliability as operation lifetime typically involves a large number of cycles in the order of  $10^7$  [2]. Recent developments of ultra-low fatigue SMA films indicate that these requirements can be met [19]. In addition to the high stability, these materials also show a low stress hysteresis resulting in high COP values larger than 10 [17, 20]. Another important issue concerns rapid heat transfer in order to achieve large heating/cooling power. Recent results indicate that the use of SMA films or foils is a promising approach as the large surface-to-volume ratios enable higher cycling frequencies [17]. These developments mark important steps towards the development of innovative heat pumping devices that combine miniaturization as well as parallelization using novel designs of highly distributed film systems.

This paper presents the design, development and characterization of first-of-its-kind demonstrators for miniaturized-scale heat pumping. Following a micro engineering approach, the investigated design concept is based on SMA bridge structures. Several layouts of mechanically coupled SMA bridges will be introduced and the performance of corresponding heat pumping devices will be evaluated. Elastocaloric materials for this investigation are TiNiFe foils with rolling-induced texture having a thickness of  $30\text{ }\mu\text{m}$ . Heat conduction through solid-to-solid contact between active material and heat source/sink will be considered for heat transfer. The interdisciplinary task of materials design, engineering and micro technology will be addressed to fully exploit the multifunctional properties of elastocaloric SMA foils.

## 2. Material and methods

Ferroic materials exhibit a structural phase transformation giving rise to large caloric effects [29–31]. Different caloric effects may be distinguished depending on the kind of field (magnetic, electric, pressure, stress) required to induce the phase transformation [11, 13]. Here, the elastocaloric effect in SMAs is of special interest that denotes the isothermal change of entropy or the adiabatic change of temperature due to a stress-induced reversible phase transformation between austenite and martensite. In particular, the elastocaloric effect is given by the release of latent heat upon loading and heat absorption upon unloading. The effect size depends on the chemical composition and microstructure of the material as well as loading and boundary conditions (strain rate, heat dissipation) [32–35]. Previous investigations mainly concentrated on Cu-based [35–37] and TiNi-based bulk SMAs [2, 28, 34, 38]. TiNi-based alloys show about the highest caloric effect amongst state-of-the-art SMA materials. The latent heat can be as high as  $31\text{ J g}^{-1}$  in the case of TiNi and  $35\text{ J g}^{-1}$  in the case of TiNi-based ternary alloys [32, 33]. The adiabatic temperature changes in these materials are in the range of 15–58 K and thus typically exceed those of the other caloric effects by an order of magnitude [13, 39, 40].

Tailoring the properties of SMA materials involves the adjustment of phase transformation temperatures. In order to prevent a thermally induced phase transformation, the austenite finish temperature  $A_f$  has to be lower than the lowest temperature that the material can reach by self-cooling during stress release. On the other hand, the critical stress to induce the austenite–martensite transformation should be below the yield stress of slip deformation to guarantee reversibility. These conditions are achieved by adding Fe to the TiNi system, which is known to shift the martensitic transformation to lower temperatures [41] and by tailoring the heat treatment conditions. In the present case, heat treatment is performed at the annealing temperature  $T_H = 450\text{ }^\circ\text{C}$ . The chemical composition is adjusted to be  $\text{Ti}_{49.1}\text{Ni}_{50.5}\text{Fe}_{0.4}$ . TiNiFe foils with a thickness of  $30\text{ }\mu\text{m}$  are produced by cold rolling with a final cold rolling reduction of 40%. The latent heat is determined by differential scanning calorimetry to about  $7.5\text{ J g}^{-1}$ .

Cold rolling induces a texture, which also affects the phase transformation and cyclic performance of the material. For tensile testing, samples with a width of 2 mm and a length of 15 mm are prepared in rolling direction (RD) and transverse direction (TD) by mechanical cutting. Samples are attached to alumina plates on both ends with a two-component adhesive. Uniaxial tensile tests are performed at different strain rates between  $10^{-4}$  and  $1\text{ s}^{-1}$  in strain-control mode. The tensile test machine is equipped with a 50 N force sensor, the resolution of the force and distance measurements are 0.25 N and  $0.25\text{ }\mu\text{m}$ , respectively. First, the sample is loaded at constant strain rate until the end of the pseudoelastic plateau is reached. This intermediate position is maintained for 10 s in order to allow for temperature equalization with the environment. Subsequently, the sample is unloaded at constant strain rate until the preload is reached. The end position is also maintained for 10 s to allow for temperature



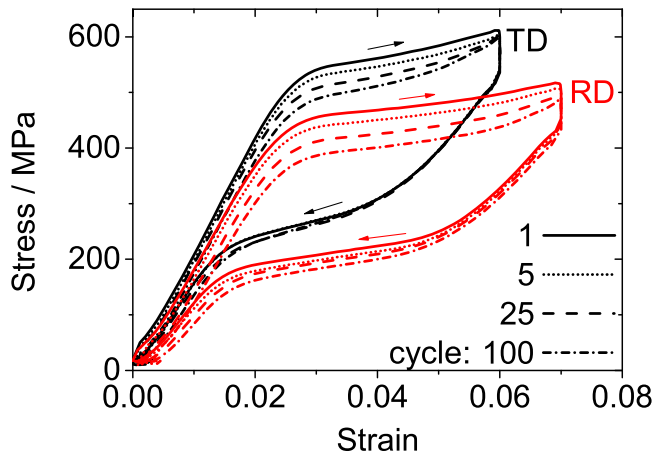


**Figure 1.** Stress–strain characteristics of pseudoelastic TiNi foil samples loaded in transversal (TD) and rolling direction (RD) at a strain rate of  $0.1 \text{ s}^{-1}$  for different cycles as indicated.

equalization. Experiments are carried out in air at room temperature. During tensile testing, the local temperature evolution of the samples is monitored *in situ* by an infrared camera with spatial resolution of  $25 \mu\text{m}$  at a frame rate of 100 Hz. Samples are covered with a thin layer of black carbon for improved thermal emissivity.

Figure 1 shows two series of tensile tests at a strain rate of  $0.1 \text{ s}^{-1}$  to analyze the cyclic mechanical performance for loading along RD and TD. The transformation strain at which the superelastic plateau ends has been determined before under quasi-static conditions. The two stress plateaus during loading and unloading correspond to the stress-induced martensitic transformation and the reverse martensitic transformation, respectively. A pronounced texture dependence of the mechanical performance occurs, which is in line with previous work [42, 43]. In RD, lower values of transformation stress and higher transformation strains are observed compared to TD.

The stress–strain characteristics depend on the cycle number. Figure 1 shows that the stress plateau of martensitic transformation and, to a lower extent, reverse transformation decreases with increasing cycle number. The largest changes occur during the first cycles, followed by a stabilization of the mechanical behavior. After 100 cycles, the loading plateau is decreased by about 15% when loading along RD. A plastic strain of 0.2% is accumulated in TD, compared to 0.35% in RD. In order to reduce the overall actuation forces and thus the requirements on the driving actuator, heat pumping will be investigated for loading direction along RD in the following. This performance is sufficient for the purpose of demonstrator development in this work. Ultimately, SMA materials will be required showing ultra-low fatigue behavior as has been shown recently [19].

By assuming work recovery during unloading, the area enclosed by the loading and unloading characteristics represents the applied mechanical work  $\Delta W$  [2, 27, 28]. For a full loading cycle along RD,  $\Delta W$  is determined to be about  $0.8 \text{ J g}^{-1}$ . It has been shown that the work increases for increasing strain rate due to an increase of hysteresis resulting

from self-heating and self-cooling during loading and unloading, respectively [17, 44, 45].

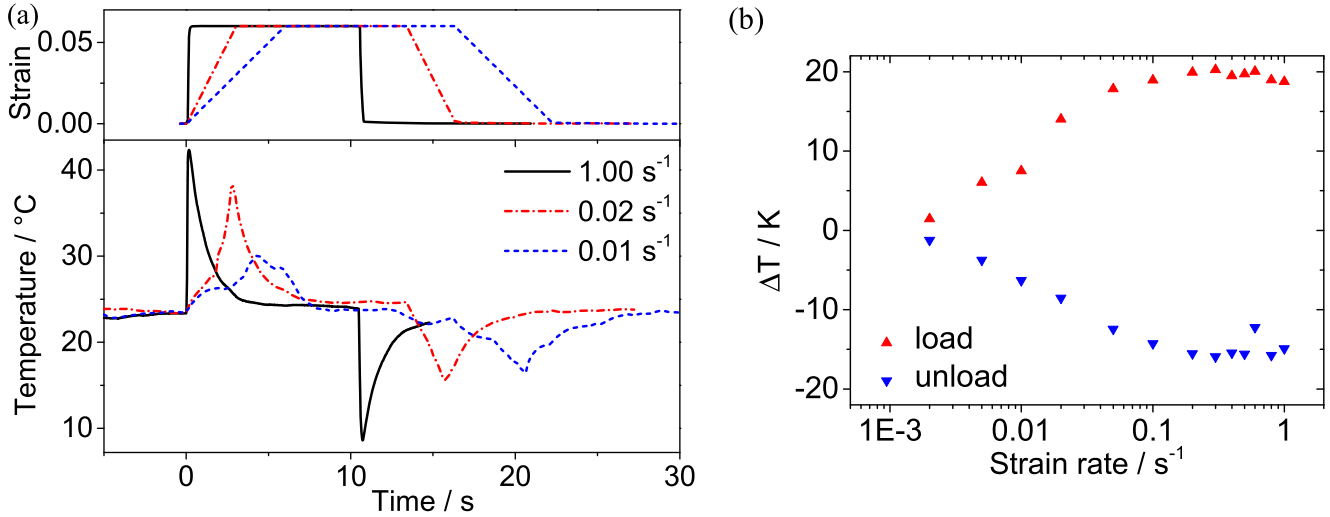
Typical results on the thermal performance during tensile experiments for several strain rates are summarized in figure 2. The time-dependent evolution of temperature is recorded by IR thermography. The temperature is averaged over a test area of  $1 \text{ mm}^2$  in the sample center. Peak temperatures  $\Delta T_{\text{load}}$  and  $\Delta T_{\text{unload}}$  are observed at the end of loading and unloading, respectively. The observed peak temperatures are summarized in figure 2(b), showing an increase of temperature change with increasing rate until the adiabatic limit is reached at the strain rate of  $0.2 \text{ s}^{-1}$ . In this case, the maximum temperature change is 20 K upon loading and  $-16 \text{ K}$  upon unloading. During intervals of constant strain, the sample temperature equalizes with the environment due to heat transfer by air convection and conduction. Corresponding time constants are determined to be about 1 s assuming an exponential temperature change.

The efficiency of the material is expressed by the coefficient of performance COP that is given by the ratio of generated heat  $Q$  and mechanical work input  $\Delta W$ . The generated heat  $Q$  is evaluated from the temperature changes  $\Delta T$  according to  $Q = c_p \cdot \Delta T$ , assuming a heat capacity  $c_p = 0.5 \text{ J g}^{-1} \text{ K}^{-1}$ . Based on the experimental results, we find material COPs of 13 and 10 for heating and cooling, respectively. These results may be compared with the Carnot efficiency  $T_{\text{hot/cold}} \cdot (T_{\text{hot}} - T_{\text{cold}})^{-1}$  indicating the ultimate limit of thermodynamic heat pumping for the cases of heating/cooling, respectively. For the given temperatures, the COPs reach about 80% and 60% of the Carnot efficiency for heating ( $T_{\text{hot}} = 316 \text{ K}$ ,  $T_{\text{cold}} = 296 \text{ K}$ ) and cooling ( $T_{\text{hot}} = 296 \text{ K}$ ,  $T_{\text{cold}} = 280 \text{ K}$ ), respectively. These values are comparable to maximum COPs obtained by vapor compression and outreach thermoelectric performance [2].

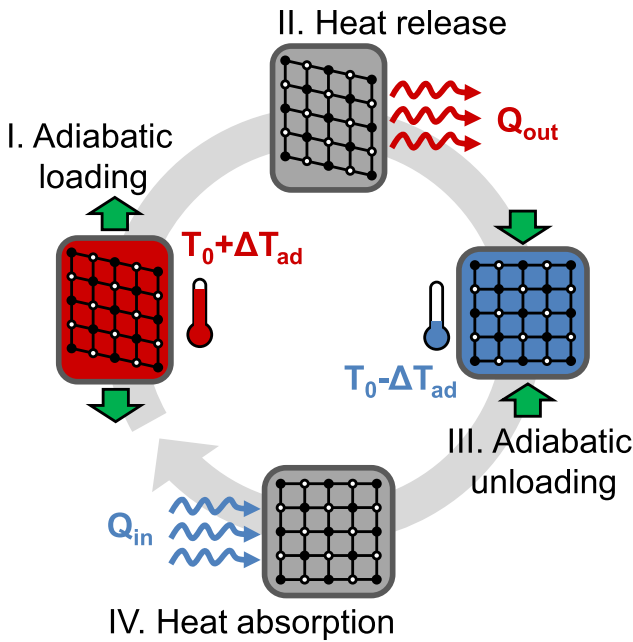
### 3. Design concept

Figure 3 shows a schematic of an elastocaloric heat pumping cycle according to a reverse Brayton process [25, 46]. Four operation steps may be distinguished as indicated. Adiabatic loading (step I) and unloading (step III) are applied to induce the exothermal martensitic phase transformation and the corresponding endothermal reverse transformation, respectively. In between the loading and unloading steps, heat needs to be transferred between active device and environment. In the tensile experiments described above, heat is exchanged via the sample fixations by heat conduction and surrounding air by natural convection. However, for heat pumping in a real device, heat source and sink have to be provided to direct the heat flows. In this paper, the active device is brought in physical contact to a heat sink to transfer extra heat  $Q_{\text{out}}$  while the device is kept in strained condition (step II) and to a heat source in released condition to absorb heat  $Q_{\text{in}}$  (step IV).

The maximum quantity of heat transferred in one cycle is given by the latent heat  $Q$  of the SMA volume undergoing phase transformation, if we assume negligible losses and zero temperature difference between source and sink. The



**Figure 2.** (a) Temperature change determined by IR thermography of a TiNiFe tensile test sample for different strain rates. Between loading and unloading step, the strain is held constant for 10 s to allow for temperature equalization with the environment. (b) Corresponding maximum temperature changes during mechanical loading and unloading as a function of strain rate. The adiabatic limit is reached at a strain rate of 0.2 s<sup>-1</sup>.



**Figure 3.** Schematic elastocaloric cycle for solid-state heat pumping. Four operation steps may be distinguished as indicated.

maximum achievable temperature difference between sink and source is equal to the adiabatic temperature change of the material  $\Delta T_{ad} = Q c_p^{-1}$ , where  $c_p$  is the heat capacity of the material.

An important question is: how to perform superelastic cycling on a miniature scale? The basic idea proposed here is to use a freely suspended SMA bridge that is moved perpendicularly to the bridge plane between a convex heat source and a flat sink and, thus, at the same time is periodically loaded by deformation of its center part in out-of-plane direction [47]. This concept is illustrated in figure 4(a) and

compared with the concept of loading by in-plane deflection (figure 4(b)).

The main advantage of out-of-plane deflection is that only a single actuation unit is required for tensile loading and unloading as well as for switching thermal contact between source and sink. The deflection angle is adjusted to the required transformation strain. As the angle is well below 45°, tensile forces dominate, while bending forces are negligible for the foil structures. The mechanical work required to drive the heat pumping cycle is illustrated by the schematic stress-strain diagrams in figure 4(c). In step I, the work  $W_{load}$  is performed to deflect the SMA bridge. This work remains stored within the material during heat release (step II). In step III, the work  $W_{unload}$  is released by the material and may be recovered for another loading step. In this case, only the work difference  $\Delta W = W_{load} - W_{unload}$  given by the area enclosed by the loading and unloading curves has to be performed for a complete elastocaloric cycle, which significantly improves device efficiency. Obviously,  $\Delta W$  can be minimized by reducing the mechanical hysteresis of transformation. In the following, layouts for heat pumping devices with enhanced device efficiency will be developed by taking work recovery into account.

#### 4. Layout and fabrication of demonstrators

In order to achieve work recovery, SMA bridges may be mechanically coupled to form antagonistic pairs of counter-acting bridges. In the following, two different layouts are considered for the development of demonstrator devices as shown in figure 5(a). The layout referred to as ‘convex layout’ is based on two SMA bridges being pre-strained with respect to each other in convex manner by a spacer in the center of the bridges (figure 5(a)). The corresponding layout comprises two flat heat sources, between which the double bridge device

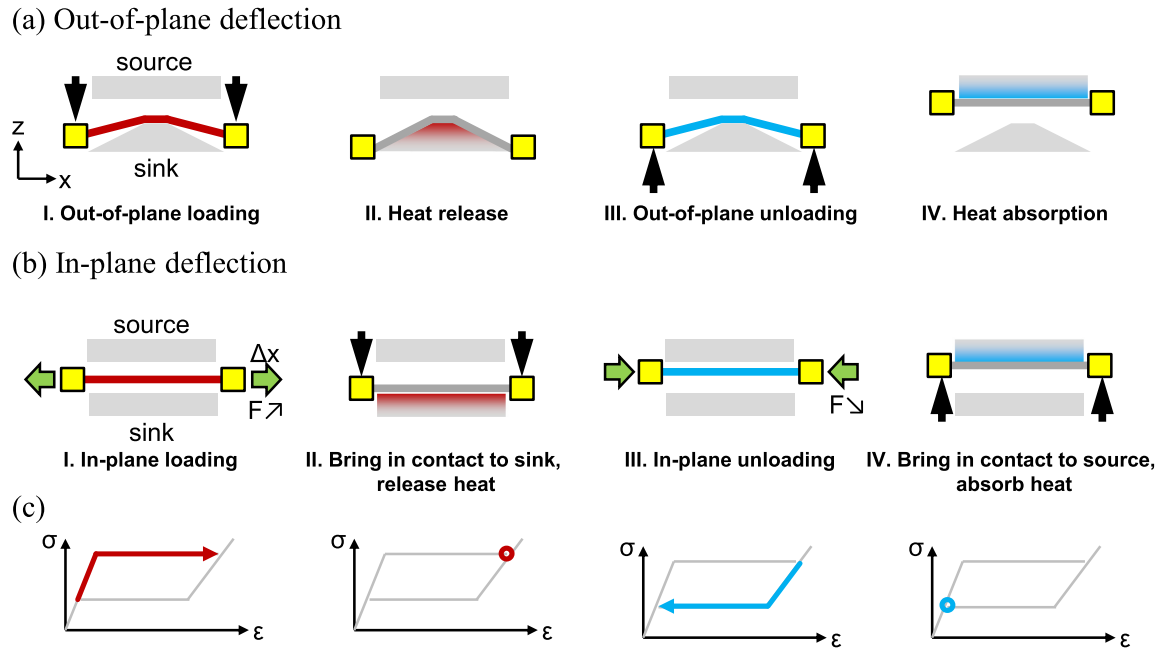


**Figure 4.** Design concepts for heat pumping based on a freely suspended SMA bridge. (a) Loading is performed out-of-plane by pressing the SMA bridge against a heat sink with convex surface. (b) Loading is performed in-plane. A second actuator is required for switching the bridge position to enable thermal contact between source and sink. (c) Schematic stress–strain diagrams illustrating the mechanical work for heat pumping.

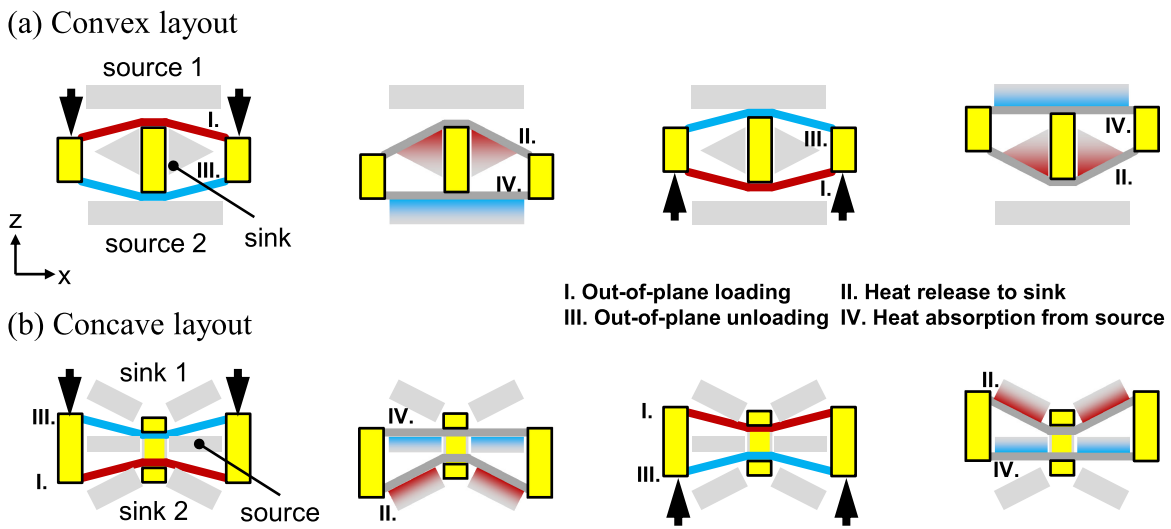


**Figure 5.** Advanced layouts of heat pumping devices based on two antagonistic SMA foil bridges mechanically coupled to each other. The four operation steps are indicated. The bridges are pre-strained with respect to each other (a) in convex manner by a spacer in the center, (b) in concave manner by a clamp in the center.

is operated periodically in out-of-plane direction ( $z$ -direction). In between both bridges, triangularly shaped heat sinks are placed, acting as a common heat sink for both bridges and significantly improving heat absorption, compared to an earlier demonstrator design [47]. During step I of the heat pumping cycle, the coupled structure is pressed against the lower heat source until full contact is established. Thereby, the upper bridge is fully loaded, whereas the lower bridge is fully relaxed. While this position is held constant for a short time interval (step II) latent heat is released from the upper bridge and heat is absorbed in the lower bridge. During the

third and fourth step, the roles of upper and lower bridge are reversed.

The layout referred to as ‘concave layout’ comprises two SMA bridges, which are pre-strained with respect to each other in concave manner by a clamp as shown in figure 5(b). Two heat sinks are arranged above and below the bridges in a proper angle to adapt to their deflection. In this case, the heat source is placed in between the bridges. In step I of the heat pumping cycle, the coupled structure is shifted downwards until the lower bridge is fully loaded and in contact to the heat sink, while the upper bridge is relaxed and in contact to the

**Table 1.** Properties and performance of elastocaloric heat pumping demonstrators based on TiNiFe foil bridges.

Layout	$C_p$ (J K <sup>-1</sup> )		$f$ (Hz)	$\Delta W$ (mJ)	$dW/dt$ (mW)	$(dT/dt)_{init}$ (K s <sup>-1</sup> )		$\Delta T$ (K)		$\tau$ (s)		$W_{heat}$ (mW)	$W_{cool}$ (mW)	COP	
	sink	source				sink	source	sink	source	sink	source			heat	cool
Single bridge	0.29	0.15	0.75	11	8.3*	0.21	-0.16	4.8	-3.1	24.9	21.0	61	24	7.3*	2.9*
Convex double bridge	64	0.32	0.76	21	16.0	0.006	-0.16	0.5	-5.0	63.0	35.4	384	51	24	3.2
Concave double bridge	0.50	0.28	0.76	19	14.4	0.14	-0.16	5.0	-4.4	34.4	30.0	70	45	4.9	3.1

Legend:  $C_p$ —heat capacity of copper segments (lumped),  $f$ —operation frequency,  $\Delta W$ —work input per cycle,  $dW/dt$ —mechanical input power,  $(dT/dt)_{init}$ —temperature change rate during first cycles (linear fit),  $\Delta T$ —temperature changes after 100 cycles,  $\tau$ —time constant for reaching steady-state conditions (exponential fit),  $W_{heat,cool}$ —estimated heating/cooling power, COP—coefficient of performance; \*work recovery is assumed.

flat heat source. This position is held constant during step II to allow for heat transfer to the lower heat sink and for absorption of heat from the heat source. Again, during the third and fourth step, the roles of upper and lower bridge are reversed. Note that the heat source is used as a common source for both bridges and, thus, it is cooled twice during each cycle.

Miniature-scale elastocaloric devices based on bridge geometries require precision machining, as well as three-dimensional integration technologies for SMA bridges, heat sources/sinks and supporting structures. Moreover, pre-straining of the bridges by spacer or clamps has to be accomplished with sufficient accuracy. In order to allow for efficient heat transfer, heat sources and sinks have to be well aligned with respect to the SMA bridges and the contacting surfaces have to match in order to obtain small thermal contact resistances [48, 49]. As small length changes due to training effects cannot be avoided, the device should be able to adapt or compensate for these effects during operation.

A special auxiliary frame is developed for three-dimensional alignment and pre-straining of single bridge devices [47]. For the convex layout, a polymer spacer is attached to the center of one bridge. Then, the second bridge is pressed and bonded onto the first one. The height of the spacer is chosen in such a way, that one bridge is subjected to the full transformation strain determined from tensile tests, while the counteracting bridge is in unstrained condition. In the present layout, a spacer height of 5 mm leads to a strain change of 4.5%. For fabrication of the concave layout, two single bridge devices are mounted with spacers in between their fixations. Then, the bridges are pre-strained towards each other by a polymer clamp in their center.

The heat sources and sinks are assembled from several individual copper segments of variable heat capacities (see table 1) in order to monitor the heat transfer with a coarse spatial resolution. In the case of the convex layout, the heat sink is fabricated from brass having a much higher mass and heat capacity, compared to the segments of the heat sources. In comparison, the heat capacity of an individual TiNiFe bridge is about  $0.0039 \text{ J K}^{-1}$ . Pt100 temperature sensors are attached to each segment. Heat sink segments are arranged with a slope of  $19.4^\circ$  with respect to the bridge plane, corresponding to a maximum strain of 4.5% within the SMA bridge when in full contact. In order to improve thermal contact, surfaces of the heat sources are also aligned with a small slope, leading to a strain of 0.5% in the relaxed bridge. This helps to compensate for small plastic deformations in the SMA bridges due to training effects. The segments are held in place by supporting structures produced from polymer resins by stereolithographic 3D-printing. These supporting structures contain spring mechanisms, which compensate for asymmetries in the assembly as well as plastic deformations in the SMA bridges. In addition, they assure that the bridges are pressed in a flat manner against the copper segments in order to provide good thermal contact between them (figure 6). The polymer springs consist of meandering stripes with a thickness of  $400 \mu\text{m}$  and a depth of 3 mm.

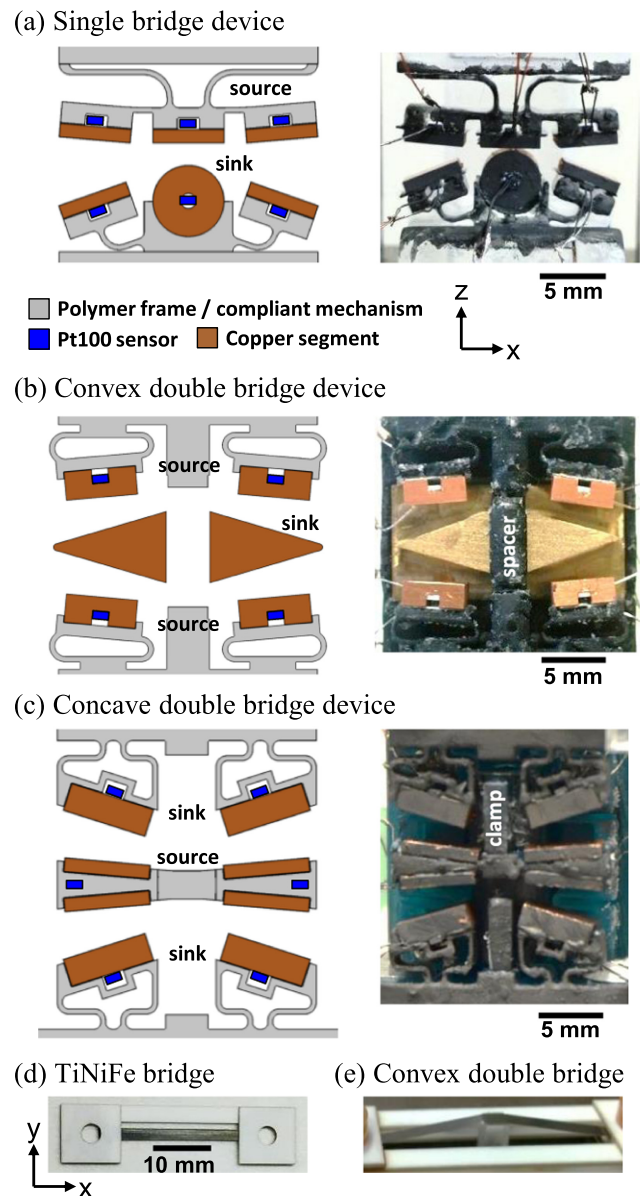


**Figure 6.** Support frame comprising polymer spring mechanisms, copper segments and Pt100 temperature sensors for (a) single bridge device, (b) convex double bridge device and (c) concave double bridge device. The thickness and depth of the spring mechanisms is  $400 \mu\text{m}$  and 3 mm, respectively. A picture of each device is shown on the right, (a), (c) with and (b) without the surfaces covered with black carbon for improved thermal emissivity. (d) TiNiFe bridge attached to alumina frame. Bridge devices are placed in between heat sources and sinks in horizontal orientation. (e) Assembled convex double bridge device with polymer spacer in bridge center.

Heat pumping demonstrators consist of a testing frame providing a linear guidance of the bridge devices in between the outer limit positions (i.e. when the devices are in full contact to heat sources/sinks). Actuation is performed by a tensile testing machine with spindle drive motor, force and displacement sensors having a maximum velocity of  $30 \text{ mm s}^{-1}$ . Pt100 sensors are read out at a frequency of 10 Hz. In addition, demonstrators are monitored with an IR camera (100 Hz) during operation. Surfaces pointing towards



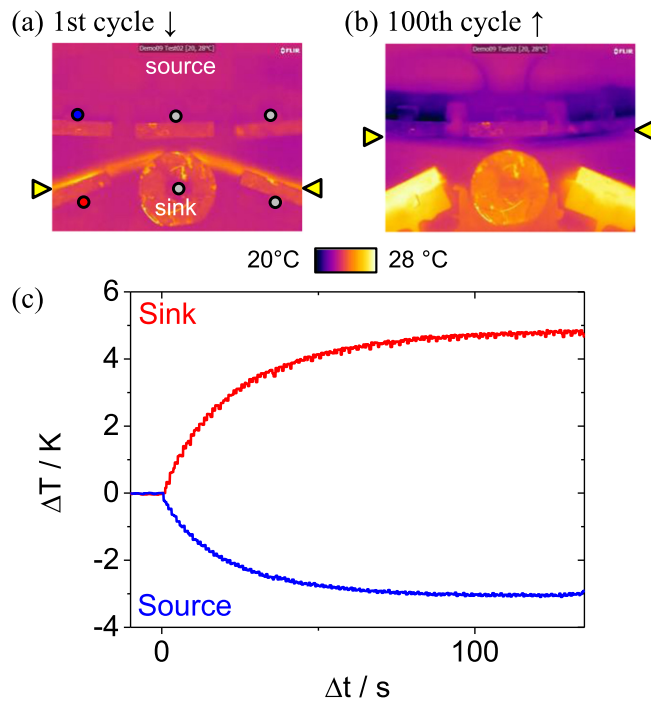


**Figure 7.** IR thermograms of a single bridge device operated at 0.75 Hz after the first (a) and hundredth (b) elastocaloric cycle. The SMA bridge, indicated by arrows, is either in contact with the heat sink or with the heat source. The position of Pt100 sensors is indicated by circles. (c) Time-dependent temperature evolution of heat sink and source taken from sensors at the left segments (red and blue circles in (a)).

the camera are covered with black carbon in order to provide uniform emissivity.

## 5. Performance characteristics

### 5.1. Single SMA bridge

A series of cyclic experiments is performed on single bridge devices in displacement control mode by operating the bridges repeatedly between heat source and sink. These experiments serve as a reference for the heat pumping demonstrators. Operation frequency is limited by the maximum velocity of  $30 \text{ mm s}^{-1}$  of the used driving actuator. The time duration of physical contact between SMA bridges and heat source/sink is about 0.3 s.

Figure 7 shows snapshots of the temperature distribution of the single bridge device for an operation frequency of 0.75 Hz after the first (a) and hundredth cycle (b). The IR thermograms show that the Cu segments of the heat source, as well as parts of the polymer support structures are cooled, whereas the heat sink is heated up. The central segment of the heat sink is heated less than the outer segments, because it has a higher heat capacity. The temperature changes registered by the individual Pt100 sensors are similar, but not equal due to slight asymmetries in the alignment. The graph in figure 7(c) shows the time-dependent temperature evolution of the heat sink and outer heat source segments. In the beginning, the

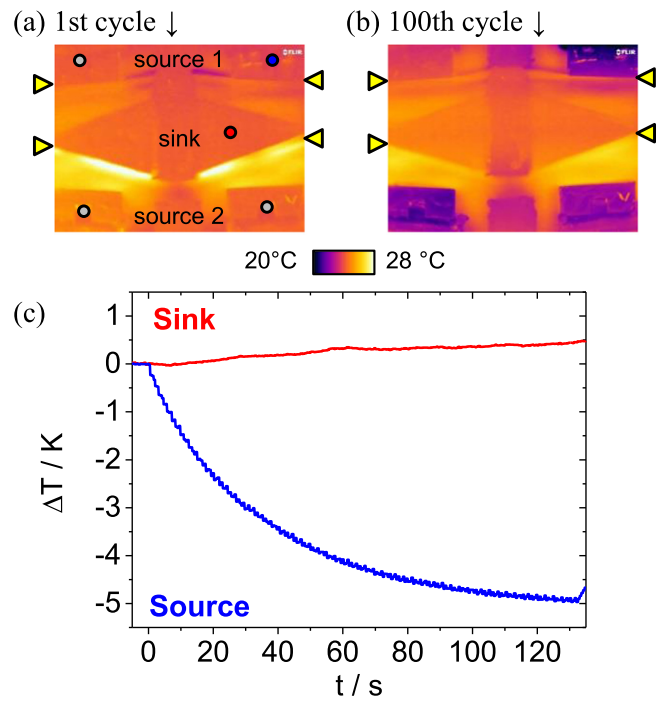


**Figure 8.** IR thermograms in the center part of a heat pump of the convex double bridge layout operated at 0.76 Hz during (a) first and (b) 100th cycle. The SMA bridges (indicated by arrows) are in contact with the heat sink and the upper heat source in both cases. The position of Pt100 sensors is indicated by circles. (c) Corresponding time-dependent temperature evolution of heat sink (red circle in (a)) and source (blue circle in (a)). The experiment is stopped after 100 cycles.

heating and cooling rates are  $0.21 \text{ K s}^{-1}$  and  $-0.16 \text{ K s}^{-1}$  for sink and source, respectively. In the following, the temperatures follow an exponentially decaying trend and approach steady-state conditions after about 65 cycles (or 100 s). In this case, the sink is heated by 4.8 K and the source cooled by  $-3.1 \text{ K}$ . The time constants, obtained by least squares fit of a single exponential are between 20 and 25 s (see table 1). Note that the sink temperature keeps slightly increasing after 100 s, presumably due to heat dissipation by irreversible processes.

### 5.2. Heat pumping demonstrators

Preliminary results on the convex layout without solid heat sink have been presented in [47], in which the surrounding air played the role of a heat sink. These investigations revealed a number of drawbacks due to insufficient heat flow indicating that fast heat transfer, e.g. through solid–solid thermal contact, is essential for efficient heat pumping. Here, we discuss the results on an improved convex layout comprising a solid heat sink. The sink is designed with a significantly larger heat capacity compared to the heat source. This allows for effective heat removal, which is of special interest for solid-state cooling. Figure 8 shows thermograms of the device operated at 0.76 Hz during the first (a) and hundredth cycle (b). After 100 cycles, the heat source segments above and below the coupled device are cooled. The smaller temperature change of

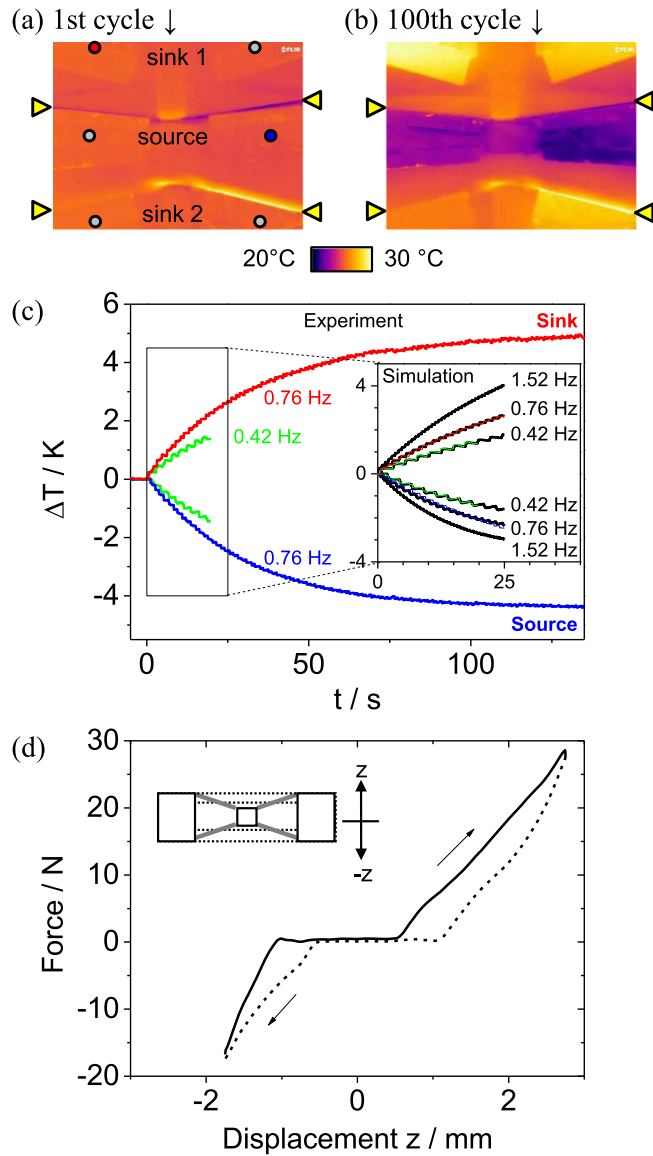


**Figure 9.** IR thermograms in the center part of a heat pump of the concave double bridge layout operated at 0.76 Hz during (a) first and (b) 100th cycle. The SMA bridges (indicated by arrows) are in contact with the heat source and the lower heat sink in both cases. The position of Pt100 sensors is indicated by circles. (c) Corresponding time-dependent temperature evolution of heat sink (red circle in (a)) and source (blue circle in (a)) during operation at two different frequencies. The experiments are stopped after 8 and 100 cycles, respectively. The inset shows the temperature evolution during the first 25 s simulated with a lumped element model of the heat transfer (see section 6). (d) Force-displacement characteristics of SMA bridges during a heat pumping cycle at a frequency of 0.1 Hz.

the upper left segment is related to slight assembly asymmetries or incomplete phase transformation of the upper SMA bridge. The upper right segment shows the highest cooling effect. The heat sink, on the other hand, is only marginally heated up due to its higher mass. Measurements of the Pt100 sensors (figure 8(c)) show that the heat source is cooled by  $-5$  K, whereas the sink is heated by  $+0.5$  K.

Results on the concave layout are presented in figure 9. In this case, heat capacities of heat sink and source are designed to be similar. Figure 9 shows snapshots of the temperature distribution in the center part of the heat pump during the first (a) and hundredth cycle (b). For increasing cycle number, the heat sinks arranged above and below the device are heated up, whereas the heat source in between both SMA bridges is cooled down. Again, the temperature changes in the individual segments are slightly different, because of asymmetries in the setup and incomplete phase transformation of the SMA bridges. The highest temperature changes are obtained in the upper left heat sink and the right heat source, respectively.

The time-dependent evolution of temperatures in these segments is shown in figure 9(c) for two operation frequencies of 0.42 and 0.76 Hz. The time durations for heat exchange, while the SMA bridges are in contact to the sink and source segments, are 0.8 and 0.3 s, respectively. At 0.76 Hz, the maximum temperature changes of sink and source are to  $+5$  K and  $-4.4$  K, respectively. In this case, stationary conditions are reached within about half a minute. The experiment at 0.42 Hz is stopped after 8 cycles revealing lower heating and cooling rates of sink and source.

The force-displacement characteristic of the concave layout is shown exemplarily in figure 9(d) for a low frequency of 0.1 Hz. Due to the layout consisting of two SMA bridges, the characteristics of the coupled devices comprise two hysteresis subloops. These subloops correspond to the displacement intervals during which the device is in mechanical contact to one of the heat sinks. Without mechanical contact, i.e. for displacements between  $-0.5$  and  $0.5$  mm, the device is force-free since the forces of the antagonistically coupled bridges compensate each other. Both bridges are in the superelastic strain range during virtually the whole operation cycle. The asymmetry of both curves in figure 9(d) is caused by slightly asymmetric loading causing a higher contact force at the upper sink. The mechanical input power, i.e. the work per time interval, is estimated based on cycling frequencies and numerical integration of the force-displacement characteristics. The work input per cycle is in the order of 10 mJ for the single bridge device (assuming that work is recovered during unloading), and 20 mJ for the convex and concave coupled double bridge devices.

The cooling and heating power of the demonstrator devices is estimated based on the heat capacity of the heat sources and sinks and the initial cooling rate (table 1), assuming that the same rate is obtained in all segments of the heat source. In a conservative calculation, only the heat capacity of the copper segments is considered, while polymer support structures are neglected. The estimated cooling power is 24 mW for the single bridge device, 51 mW for the convex layout and 45 mW for the concave layout. The heating powers are higher in all cases. A major reason is that dissipation and friction losses contribute to heating but counteract cooling. Another reason is that heat sinks have been designed with

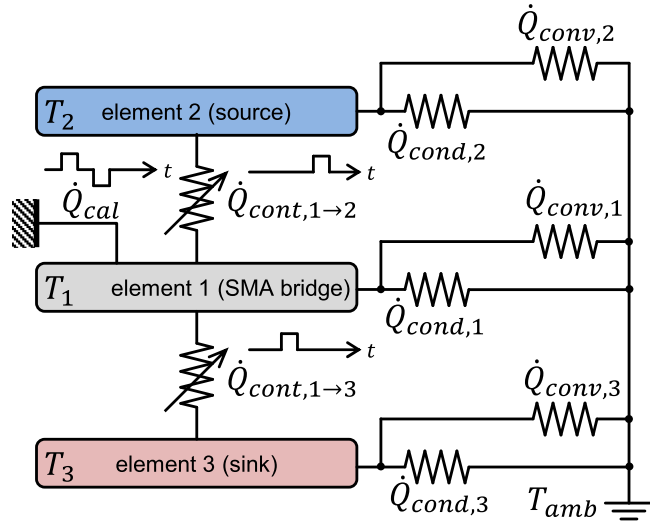


**Figure 10.** Lumped element model of heat transfer in elastocaloric heat pumping demonstrators. The values of heat release and absorption in the SMA bridge (element 1) due to the elastocaloric effect are implemented by a time-dependent heat flow  $\dot{Q}_{cal}$  proportional to the strain rate  $\dot{\epsilon}$ . Heat flows  $\dot{Q}_{cont,1 \rightarrow 2,3}$  between SMA bridge and source (element 2)/sink (element 3) are alternately switched on and off after loading/unloading, respectively. Thermal losses due to air convection and conduction through the frame are considered by convective and conductive heat flows  $\dot{Q}_{conv,\alpha}$  and  $\dot{Q}_{cond,\alpha}$  for all three elements ( $\alpha = 1, 2, 3$ ). Heat flows are proportional to heat transfer coefficients, effective surfaces and temperature differences.

higher masses/volumes compared to heat sources, hence parasitic heat flow through the surfaces is less dominant.

Based on cooling/heating power and work input, the COPs are calculated for the three devices. The COP for cooling is 2.9 for the single bridge device, 3.2 for the convex layout and 3.1 for the concave layout. Note that recovery of work is presumed for the single bridge device, whereas it is readily implemented for the coupled devices. The heating COPs are higher in all cases: 7.3 for the single bridge, 24 for the convex layout and 4.9 for the concave layout. Higher values for heating than for cooling are expected, since dissipation and friction losses also contribute to heating. In addition, the Carnot COP is always higher for heating than for cooling assuming the same temperature difference. The extraordinarily high heating COP for the convex layout is due to the high heat capacity of the sink compared to the active material resulting in a small temperature increase by only 0.5 K.

## 6. Discussion

The presented results demonstrate the large potential of miniaturization and microtechnology-compatible design to realize a new generation of heat pumping devices with large heating and cooling power at small mechanical input power. Major requirements for elastocaloric heat pumping comprise a large adiabatic change of temperature  $\Delta T_{ad}$ , reversibility over

a large number of operation cycles, rapid heat transfer as well as low work input. These requirements lead to conflicting design criteria, as a large overall latent heat obviously leads to designs with large sample mass, which in turn hampers rapid heat transfer. The use of SMA films and foils with large surface-to-volume ratio is a promising approach to solve this conflict. In particular, large contact areas can be designed allowing for rapid heat transfer at time constants well below a second when mechanically contacting a heat source or sink, which significantly boosts heat pumping power.

Besides thermal optimization, minimization of mechanical input power is of equal importance to enable a large coefficient of performance on the device level. SMA materials showing small hysteresis are of special interest to meet this goal [50, 51]. However, bulk materials pose severe requirements on the force and stroke of the driving actuator. This problem can be mitigated by using SMA films or foils as they offer new design solutions combining simplicity and large efficiency. Here, we present freely suspended SMA bridge designs that only require a single actuation unit for tensile loading and unloading as well as for switching thermal contact between source and sink. By mechanically coupling SMA bridges to form antagonistic pairs of counteracting subunits, work recovery can be achieved to improve device efficiency.

These new concepts are demonstrated for miniature heat pumping devices based on textured TiNiFe foils of 30  $\mu\text{m}$  thickness. However, the results are of equal importance for larger-scale applications. These profit from short heat transfer times in just the same way and may be obtained by increasing the number and lateral dimensions of the devices without increasing the thickness of the active material. The investigated material exhibits self-heating and -cooling of +20 and -16 K, respectively. This large caloric effect allows for high mass ratios between the active material and the reservoir to be heated or cooled in a single cycle. The texturing produced by cold rolling stabilizes the martensitic microstructure, resulting in minor training effects during the first superelastic cycles and low functional fatigue. During the first hundred cycles, small plastic strain is accumulated that can be compensated by device design.

Fabrication on the miniature scale involves specific design and manufacturing routes. Fabrication of SMA bridges is performed by precision machining that enables a smooth surface finish with high structural stability. Mechanical coupling of SMA bridges requires a three-dimensional assembly based on the precise integration of spacers and/or clamps to maintain given strain limitations. The contacting surfaces of SMA bridges and heat sources and sinks have to be well aligned to allow for efficient heat transfer. We demonstrate that the design and integration of compliant spring mechanisms is helpful to compensate for asymmetries in the assembly as well as plastic strain accumulation during cyclic operation.

The observed time constant for temperature equalization of a freely suspended SMA bridge of 30  $\mu\text{m}$  thickness in air is about 1 s, which is orders of magnitude faster than for wire or other bulk geometries [2, 22]. Hence, heat exchange with heat source and sink in a miniature-scale heat pumping device has

to be considerably faster in order to utilize the full potential of the active material. In the present study, the shortest interval that has been investigated with the current experimental setup is 0.3 s. In this case, the achieved maximum temperature difference is 9.4 K (concave layout) and the maximum cooling is  $-5$  K (convex layout), which outperforms current elastocaloric demonstrators [23, 52]. Corresponding maximum values on power and device COP of heating/cooling are 70/45 mW and 4.9/3.1 (concave layout), respectively. This important result underlines the potential of miniaturization and microtechnology-compatible design. In addition, it demonstrates that both the material and design aspect are crucial for demonstrator development. In these results, the work of the driving actuator is not taken into account. While electromagnetic motors may be considered for macroscopic devices, piezo motors having efficiencies up to 0.7 seem to be appropriate for microcooling applications. The use of MEMS actuators is not foreseen as the demands on forces and strokes are rather high.

For better understanding of heat transfer effects, a lumped element model of the demonstrators has been implemented as illustrated in figure 10. Heat flows at the different thermal interfaces have been calculated based on device geometries and estimated heat transfer coefficients. The model considers the heat capacities of the SMA bridge, sink and source segments, as well as latent heat and strain range in the stress plateau of martensitic transformation (see figure 1). The rates of heat release and absorption are proportional to the strain rate for the strain within the respective phase transformation plateaus. The heat transfer coefficients for the contact between SMA bridge and heat source, as well as SMA bridge and heat sink are adjusted to be 300 and  $1200 \text{ W m}^{-2} \text{ K}^{-1}$  for best agreement with the experimental results. The higher heat transfer to the heat sink is attributed to the higher contact force of the fully stressed SMA bridge. Convective heat transfer at the free surfaces of the SMA bridge is described by a heat transfer coefficient of  $5 \text{ W m}^{-2} \text{ K}^{-1}$ . Additional heat transfer coefficients are introduced for heat sink and source to take conductive losses to the polymer frame into account. Simulation results are included in the inset of figure 9(c) showing good agreement with experimental results for the frequencies 0.42 and 0.76 Hz. In addition, the inset includes a simulation for an even higher frequency of 1.52 Hz revealing further increase of heat pumping rate and temperature change due to lower impact of parasitic heat exchange with the environment. This result demonstrates that significant performance improvement is expected by increasing the cycling rate, which has been limited in the current experimental setup to frequencies below 0.8 Hz. The simulations also show that a larger temperature change is possible by further minimizing parasitic heat transfer to the environment, e.g., by employing materials with better thermal insulation or by operating the device in vacuum.

The presented results are obtained from a first generation of demonstrator devices. Further detailed mechanical and thermal design studies will be required to exploit the full potential of the new heat pumping concept. An ongoing issue

is the further tailoring of film and foil materials. Estimating the maximum adiabatic temperature change based on maximum reported values of latent heat in the order of  $30 \text{ J g}^{-1}$  in TiNi-based alloys [32, 33], temperature changes could be as high as 60 K, which is in line with maximum experimental values [39]. In addition, requirements on functional and structural fatigue are severe. Therefore, recent developments on ultra-low fatigue materials need to be further extended in order to enlarge the portfolio of suitable materials [19]. This research is strongly interlinked with the ongoing search for low-hysteresis materials that allow keeping the work input small.

A number of issues are related to mechanical and thermal design. Two different coupling schemes have been proposed that could serve as building blocks for larger stacks of coupled bridges being operated in parallel and consisting of alternating sinks and sources. While the manufacturing differs for both coupling schemes, performances are expected to be similar. Heat transfer rates strongly depend on the thermal resistance between the solid bodies brought into contact with each other. Therefore, further means of improving the device performance could be the increase of contact area and contact forces, possible surface treatments to reduce surface roughness and the deposition of additional thermally conductive surface coatings. Further design optimization includes adaptation to operation conditions and time-dependent effects such as relaxation.

The theoretical maximum temperature difference between source and sink is limited by the material's adiabatic temperature change  $\Delta T_{\text{ad}}$  of 16 K for the presented layouts. This temperature difference may not be sufficient for certain applications. Temperature differences beyond the adiabatic temperature change are accessible by operating several devices in a cascade comprising multiple stages. Additional limitations may arise for specific application temperatures due to limited tunability of phase transformation temperatures. A further route for future improvements of miniature heat pumps is implementing the concept of active regeneration to create a temperature gradient between heat source and sink [24, 27]. A variety of active magnetic regeneration demonstrators based on magnetocaloric materials have been implemented during the last decades [53–55]. In general, these concepts rely on a working fluid and a fluid control system. However, recently a prototype of an electrocaloric [56] and simulation studies of a magnetocaloric microcooler [57] were presented, which are entirely solid state-based.

In practical applications, heat pumps are either designed for cooling or for extracting heat from a lower temperature level. While in the first case, the heat sink temperature should ideally be kept at ambient level, in the latter case the same applies to the heat source. In order to achieve a more efficient heat transfer, a serial combination of the miniature-scale heat pump with passive heat transport structures like micro-channels or micro-heat exchangers may be considered [58–60].



## 7. Conclusions

SMA foils/films and corresponding micro-engineering concepts offer new prospects for heat pumping. The large caloric effect and multifunctional properties of these materials are used in an optimum way by designing for large surface-to-volume ratios and large contact areas between the materials and heat source/sink as well as by mechanically coupling the materials to form counteracting subunits. By introducing SMA bridge structures and implementing these design concepts, we demonstrate rapid heat transfer as well as work recovery resulting in large heating and cooling power at small mechanical input power.

The demonstrators presented here consist of superelastic TiNiFe shape memory foils. Free-standing TiNiFe bridges are coupled to antagonistic pairs, which allows for operation by a single linear actuator to induce phase transformation and thermal contact switching between the bridge structures and heat source/sink. While the self-heating and -cooling of the material due to stress-induced phase transformation is +20 K and −16 K, respectively, corresponding demonstrators achieve a temperature difference of 9.4 K between heat source and sink which is competitive with or surpasses current macro-scale elastocaloric devices [23, 52]. The heating and cooling power are 70 and 45 mW (in the case of heat source and sink having similar heat capacities). When normalizing these values to the mass of active material, the values for the specific heating and cooling power of 4.5 and 2.9 W g<sup>−1</sup> are obtained. The device COPs of heating and cooling are 4.9 and 3.1, respectively. These numbers outperform state-of-the-art thermoelectric coolers, having COPs below 2.5 in most cases [9].

Therefore, the introduced technology has great potential to improve efficiency and reduce energy consumption in various temperature control applications. Based on the presented results, also larger-scale applications can be foreseen, e.g. in household. Devices may be operated either stand-alone, or used as building blocks for larger, distributed systems. In either case, heat transfer will be highly improved by the use of active material with large surface-to-volume ratio.

## Acknowledgments

The authors (H Ossmer and M Kohl) gratefully acknowledge funding by the German Science Foundation (DPG) within the priority program SPP1599 ‘Caloric Effects in Ferroic Materials: New Concepts for Cooling’ [61].

## References

- [1] Goetzler W, Zogg R, Young J and Johnson C 2014 *Energy Savings Potential and RD&D Opportunities for Non-Vapor-Compression HVAC Technologies* Navigant Consulting, Inc. (prepared for US Department of Energy) (<http://energy.gov/sites/prod/files/2014/03/f12/Non-Vapor%20Compression%20HVAC%20Report.pdf>)
- [2] Cui J, Wu Y, Muehlbauer J, Hwang Y, Radermacher R, Fackler S, Wuttig M and Takeuchi I 2012 *Appl. Phys. Lett.* **101** 073904
- [3] Carmo J P, Silva M F, Ribeiro J F, Wolffenbuttel R F, Alpuim P, Rocha J G, Goncalves L M and Correia J H 2011 *Microsyst. Technol.* **17** 1283–91
- [4] El-Ali J, Perch-Nielsen I R, Poulsen C R, Bang D D, Telleman P and Wolff A 2004 *Sensors Actuators A* **110** 3–10
- [5] Chu R C, Simons R E, Ellsworth M J, Schmidt R R and Cozzolino V 2004 *IEEE Trans. Device Mater. Reliab.* **4** 568–85
- [6] Majumdar A 2009 *Nat. Nanotechnol.* **4** 214–5
- [7] Riffat S B and Ma X 2003 *Appl. Therm. Eng.* **23** 913–35
- [8] Bell L E 2008 *Science* **321** 1457–61
- [9] He W, Zhang G, Zhang X, Ji J, Li G and Zhao X 2015 *Appl. Energy* **143** 1–25
- [10] Vining C B 2009 *Nat. Mater.* **8** 83–5
- [11] Fähler S, Röbber U K, Kastner O, Eckert J, Eggeler G, Emmerich H, Entel P, Müller S, Quandt E and Albe K 2012 *Adv. Eng. Mater.* **14** 10–9
- [12] Mañosa L, Planes A and Acet M 2013 *J. Mater. Chem. A* **1** 4925–36
- [13] Moya X, Kar-Narayan S and Mathur N D 2014 *Nat. Mater.* **13** 439–50
- [14] Takeuchi I and Sandeman K 2015 *Phys. Today* **68** 48–54
- [15] Moya X, Defay E, Heine V and Mathur N D 2015 *Nat. Phys.* **11** 202–5
- [16] Kitanovski A, Plaznik U, Tomc U and Poredoš A 2015 *Int. J. Refrig.* **57** 288–98
- [17] Ossmer H, Lambrecht H, Gültig M, Chluba C, Quandt E and Kohl M 2014 *Acta Mater.* **81** 9–20
- [18] Bechtold C, Chluba C, Lima de Miranda R and Quandt E 2012 *Appl. Phys. Lett.* **101** 091903
- [19] Chluba C, Ge W, Lima de Miranda R, Strobel J, Kienle L, Quandt E and Wuttig M 2015 *Science* **348** 1004–7
- [20] Ossmer H, Chluba C, Güeltig M, Quandt E and Kohl M 2015 *Shape Mem. Superelasticity* **1** 142–52
- [21] Chluba C, Ossmer H, Zamponi C, Kohl M and Quandt E 2016 *Shape Mem. Superelasticity* **2** 95–103
- [22] Ossmer H, Miyazaki S and Kohl M 2015 *Mater. Today: Proc.* **2S** S971–4
- [23] Schmidt M, Schütze A and Seelecke S 2015 *Int. J. Refrig.* **54** 88–97
- [24] Qian S, Ling J, Muehlbauer J, Hwang Y and Radermacher R 2015 *Int. J. Refrig.* **55** 102–19
- [25] Qian S, Ling J, Hwang Y, Radermacher R and Takeuchi I 2015 *Int. J. Refrig.* **56** 65–80
- [26] Qian S, Alabdulkareem A, Ling J, Muehlbauer J, Hwang Y, Radermacher R and Takeuchi I 2015 *Int. J. Refrig.* **57** 62–76
- [27] Tušek J, Engelbrecht K, Millán-Solsona R, Mañosa L, Vives E, Mikkelsen L P and Pryds N 2015 *Adv. Energy Mater.* **5** 1500361
- [28] Schmidt M, Ullrich J, Wiecek A, Frenzel J, Schütze A, Eggeler G and Seelecke S 2015 *Shape Mem. Superelasticity* **1** 132–41
- [29] Pecharsky V K and Gschneider K A 1997 *Phys. Rev. Lett.* **78** 4494–7
- [30] Mischenko A S, Zhang Q, Scott J F, Whatmore R W and Mathur N D 2006 *Science* **311** 1270–1
- [31] Planes A and Mañosa L 2001 *Solid State Physics* vol 55 (New York: Academic) p 159
- [32] Otubo J, Rigo O D, Coelho A A, Neto C M and Mei P R 2008 *Mater. Sci. Eng.* **481–482** 639–42
- [33] Frenzel J, Wiecek A, Opahle I, Maaß B, Drautz R and Eggeler G 2015 *Acta Mater.* **90** 213–31
- [34] Pieczyska E A, Gadaj S P, Nowacki W K and Tobushi H 2006 *Exp. Mech.* **46** 531–42

- [35] Bonnot E, Romero R, Mañosa L, Vives E and Planes A 2008 *Phys. Rev. Lett.* **100** 125901
- [36] Mañosa L, Planes A, Vives E, Bonnot E and Romero R 2009 *Funct. Mater. Lett.* **02** 73–8
- [37] Mañosa L, Jarque-Farnos S, Vives E and Planes A 2013 *Appl. Phys. Lett.* **103** 211904
- [38] Tušek J, Engelbrecht K, Mikkelsen L P and Pryds N 2015 *J. Appl. Phys.* **117** 124901
- [39] Pieczyska E A, Tobushi H and Kulasinski K 2013 *Smart Mater. Struct.* **22** 035007
- [40] Lu B F and Liu J 2015 *Sci. Bull.* **60** 1638–43
- [41] Wang F E, Buehler W J and Pickart S J 1965 *J. Appl. Phys.* **36** 3232–9
- [42] Kim K and Daly S 2013 *Smart Mater. Struct.* **22** 075012
- [43] Sittner P, Liu Y and Novak V 2005 *J. Mech. Phys. Solids* **53** 1719–46
- [44] He Y J, Yin H, Zhou R H and Sun Q P 2010 *Mater. Lett.* **64** 1483–6
- [45] He Y J and Sun Q P 2011 *Int. J. Solids Struct.* **48** 1688–95
- [46] Plaznik U, Tusek J, Kitanovski A and Poredos A 2013 *Appl. Therm. Eng.* **59** 52–9
- [47] Ossmer H, Miyazaki S and Kohl M 2015 *Proc. Transducers, Anchorage* pp 726–9
- [48] Gotsmann B and Lantz M A 2013 *Nat. Mater.* **12** 59–65
- [49] Bahrami M, Yovanovich M M and Culham J R 2005 *Int. J. Heat Mass Transfer* **48** 3284–93
- [50] Cui J et al 2006 *Nat. Mater.* **5** 286–90
- [51] Zarnetta R et al 2010 *Adv. Funct. Mater.* **20** 1917–23
- [52] Qian S, Wu Y, Ling J, Muehlbauer J, Hwang Y, Takeuchi I and Radermacher R 2015 *Proc. 24th IIR Int. Congress of Refrigeration (Yokohama, Japan)* p 2244
- [53] Rowe A 2012 *Cryogenics* **52** 111–8
- [54] Yu B F, Gao Q, Zhang B, Meng X Z and Chen Z 2003 *Int. J. Refrig.* **26** 622–36
- [55] Yu B F, Liu M, Egolf P W and Kitanovski A 2010 *Int. J. Refrig.* **33** 1029–60
- [56] Gu H M, Qian X S, Li X Y, Craven B, Zhu W Y, Cheng A, Yao S C and Zhang Q M 2013 *Appl. Phys. Lett.* **102** 122904
- [57] Silva D J, Bordalo B D, Pereira A M, Ventura J and Araújo J P 2012 *Appl. Energy* **93** 570–4
- [58] Darabi J and Ekula K 2003 *Microelectron. J.* **34** 1067
- [59] Chaudhry H N, Hughes B R and Ghani S A 2012 *Renew. Sustainable Energy Rev.* **16** 2249–59
- [60] Brandner J J, Bohn L, Henning T, Schygulla U and Schubert K 2011 *Heat Transfer Eng.* **28** 761–71
- [61] [www.ferroiccooling.de](http://www.ferroiccooling.de)